Author's Accepted Manuscript

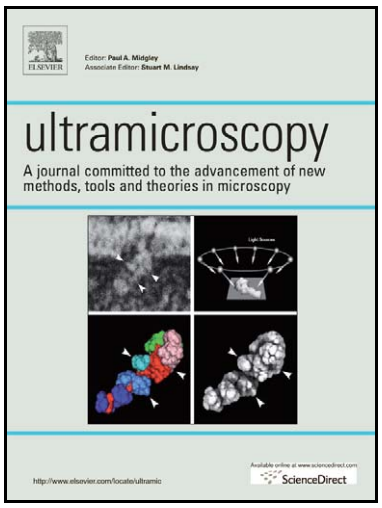

www.elsevier.com/locate/ultramic

A high speed area detector for novel imaging techniques in a scanning transmission electron microscope

T. Caswell, P. Ercius, M.W. Tate, A. Ercan, S.M. Gruner, D.A. Muller

PII: S0304-3991(08)00326-4
DOI: doi:10.1016/j.ultramic.2008.11.023
Reference: ULTRAM 10756

To appear in: *Ultramicroscopy*

Received date: 4 April 2008
Revised date: 19 November 2008
Accepted date: 28 November 2008

Cite this article as: T. Caswell, P. Ercius, M.W. Tate, A. Ercan, S.M. Gruner and D.A. Muller, A high speed area detector for novel imaging techniques in a scanning transmission electron microscope, *Ultramicroscopy* (2008), doi:10.1016/j.ultramic.2008.11.023

A High Speed Area Detector for Novel Imaging Techniques in a Scanning Transmission Electron Microscope

T. Caswell*, P. Ercius**, M.W. Tate*, A. Ercan**, S.M. Gruner*, D.A. Muller**

* Physics, Cornell University, 162 Clark Hall, Ithaca, NY, 14853
** Applied and Engineering Physics, Cornell University, E13 Clark Hall, Ithaca, NY, 14853

Keywords: Scanning transmission electron microscope; STEM; Pixel Array Detector; PAD; Diffraction imaging; Crystal grain differentiation; Copper

Abstract

A scanning transmission electron microscope (STEM) produces a convergent beam electron diffraction pattern at each position of a raster scan with a focused electron beam, but recording this information poses major challenges for gathering and storing such large data sets in a timely manner and with sufficient dynamic range. To investigate the crystalline structure of materials, a 16x16 analog pixel array detector (PAD) is used to replace the traditional detectors and retain the diffraction information at every STEM raster position. The PAD, unlike a charge-coupled device (CCD) or photomultiplier tube (PMT), directly images 120-200keV electrons with relatively little radiation damage, exhibits no afterglow and limits crosstalk between adjacent pixels. Traditional STEM imaging modes can still be performed by the PAD with a 1.1kHz frame rate, which allows post-acquisition control over imaging conditions, and enables novel imaging techniques based on the retained crystalline information. Techniques for rapid, semi-automatic crystal grain segmentation with sub-nanometer resolution are described using cross-correlation, sub-region integration, and other post-processing methods.

1 Introduction

The focused electron beam of a scanning transmission electron microscope (STEM) interacts with sub-nanometer sized material volumes to form diffraction patterns at every raster position. It is therefore capable of rapidly producing detailed and localized crystal structure information from the target

material. Standard single-channel post-specimen electron detectors integrate all transmitted electrons scattered within their subtended solid angle to form the image intensity associated with each raster position. The electron spatial distribution is integrated, thereby losing the rich diffraction information which could be used to index the material's crystal structure. Rapid acquisition of the transmitted diffraction patterns allows novel STEM imaging techniques based on a material's crystalline structure at each raster position.

Charge-coupled device (CCD) cameras have been used with STEMs to acquire high resolution diffraction patterns [1,2], but are not optimized for this imaging mode. They use a phosphor screen to convert high energy electrons (HEEs) to photons which are imaged by the CCD, because direct HEE exposure damages the CCD chip. Photon scatter within the phosphor broadens the detector point spread function (PSF), thus degrading resolution, and high radiation doses can temporarily or permanently damage the phosphor. Further, CCD chip frame rates, typically 2-30Hz or slower, are insufficient to complete a high quality STEM raster scan in a reasonable amount of time.

Most CCD camera systems are designed to acquire images in real space, but their attributes are contrary to the needs of diffraction imaging in a STEM. Real space images consist of compact, detailed information requiring high pixel density detectors, but each pixel's intensity usually varies little from its neighbors or the average. In contrast, diffraction patterns typically contain highly localized, relatively sparse information in the form of peaks with exponentially varying intensities. Therefore, STEM diffraction imaging tolerates low pixel densities to capture the discrete peaks but requires a large dynamic range for optimal sensitivity.

We have integrated a STEM and a 16x16 pixel array detector (PAD) [3, 4] to image the transmitted electron diffraction pattern at each raster position. The PAD directly images an electron beam of up to 200keV with relatively little damage and limited cross-talk between adjacent pixels. The pixel density is sufficient to identify individual diffraction peaks with a 1.1kHz frame rate. While this is slower than typical STEM scan rates, the number of channels being collected is significantly higher. The additional crystalline information retained at each raster position, as compared to traditional STEM detectors, enables novel imaging modes useful for crystal grain differentiation.

2 Detector Design and Operation

PADs consist of a photodiode array bump bonded to an application specific integrated circuit (ASIC) and directly converts incident radiation to voltage. Each photodiode is directly connected to the input of an ASIC pixel, which continuously integrates the generated charge during exposure. No mechanical shutter is necessary, because the exposure time is controlled electronically with the ASIC. High frame rates are achieved by alternating between two of the ASIC's storage elements allowing continuous data acquisition by integrating with one element while reading out the other. [4]

The PAD tested was developed as a prototype large area X-ray detector [5] and adapted for use in an electron microscope. Figure 1 shows a cross-sectional view (not to scale) of one pixel of the 300μm high resistivity Si photodiode with labeled dimensions. A 0.1μm thick metal contact layer deposited on the surface is used to apply a reverse bias of approximately twice the voltage required to fully deplete the Si photodiode. The strong electric field produced quickly separates electron-hole pairs generated by incident HEEs to reduce recombination losses and collection times. The ASIC collects the generated charge via p+ implants at the photodiode's base that segment the photodiode's active area into $(150\mu m)^2$ pixels. The diffusion length of the generated holes in the detection layer is larger than any undepleted regions that may exist between pixels, and 100% of the detector surface is active. [4]

HEEs are capable of damaging the ASIC if they penetrate through the diode layer. For electrons traveling at typical STEM accelerating voltages, the continuous slowing down approximation (CSDA) estimates a maximum path length of less than 300μm in Si [6], which estimates their maximum depth reached in the worst-case (assuming no lateral scattering) to be less than the photodiode thickness. Therefore, the photodiode stops practically all HEEs from reaching the ASIC and greatly reduces radiation damage. No radiation damage was observed in the PAD tested, and similar results were reported by McMullan, *et. al.*[7].

Figure 2 shows nested contours containing 5%, 10%, 50%, 75%, 90% and 99% (inner to outer respectively) of the deposited energy from Monte-Carlo electron scattering simulations of 5×10^6 electrons using a custom written Monte-Carlo electron scattering simulation based on Joy's work and

including relativistic corrections [8]. These contours indicate the extent of energy deposition within the detector, and only 1% of all incident electron energy is deposited outside the outermost contour. Figures 2a) and 2b) show cross-sectional views of the contours for 120keV and 200keV electrons, indicating that all HEEs deposit all of their energy before reaching the ASIC. This is consistent with the previous worst-case CSDA prediction and our experimental observations showing no detector damage after exposure to high electron flux for approximately 10 hours at the energies tested.

A FEI Tecnai F20 200keV and a FEI Tecnai T12 120keV STEM were used to test the capabilities of the PAD as a STEM electron detector. The detector is housed in a modified Fischione model-3000 high angle annular dark field (HAADF) detector canister for insertion into the microscope column.

3 Beam Spreading and Consequences for Resolution

The extent of electron scatter within the photodiode is an important estimate of the detector PSF and ultimately limits the minimum suitable pixel size. Incident HEEs randomly scatter during elastic and inelastic interactions with the diode layer's atoms resulting in wide lateral energy deposition. The average energy cost to create an electron-hole pair is 3.6eV resulting in the generation of over 30,000 electron-hole pairs per incident HEE [9]. Tests with x-rays [13], which rarely scatter laterally within Si, indicate holes are collected by the pixel in which they are generated. Lateral energy deposition due to HEE scattering therefore gives a good indication of the detector PSF in a STEM. Figures 2c) and 2d) show the energy deposition contours from above for 120keV and 200keV electrons incident on a pixel center. The 200keV electrons deposit a significant amount of energy beyond the pixel borders, but energy from 120keV electrons is mainly contained within one pixel. Electrons incident near a pixel edge will on average deposit energy within the adjacent pixels, which can allow for sub-pixel localization of a diffraction peak. Most experiments were conducted with the T12 120keV STEM due to the smaller PSF.

The ASIC continues to collect charge even after the integrator is saturated and sinks the excess to ground via leakage pathways. Pixel saturation due to intense diffraction peaks does not affect surrounding pixels as shown in figure 4 with logarithmic intensity values to show low intensity variations. The PAD therefore does not require a beam stop to block the main beam during normal STEM operation. Unless

precautions are taken, CCDs require the main beam be blocked, because of the risk of damage to the scintillator and excess charge in saturated pixels spreads to the surrounding area.

4 Detector Characterization

The ability of the PAD to image HEEs was characterized in a number of ways. A detector should ideally respond linearly to incident electron flux to produce quantitative information. Figure 3 shows the linear count response of the PAD for a given integration time over its full dynamic range as its active area was evenly illuminated with electrons. The maximum integration time for this electron flux is 4ms after which the ASIC saturates. The pixels have relatively shallow well depths of 1,200 and 2,000 HEEs at 200keV and 120keV respectively, because the ASIC electronics were originally designed for 10-14keV X-rays that each deposit approximately 90% less energy. A PAD specifically designed for STEM electron detection would exhibit a larger well depth. However, this prototype is sufficient to demonstrate the technology.

Afterglow is a common drawback of phosphor coupled CCD systems. It occurs when the phosphor is exposed to a high intensity electron beam and continues to produce photons, sometimes for hours, causing image artifacts in subsequent exposures. The PAD avoids this problem, because it directly converts incident HEEs into charge that is rapidly removed from the diode layer after generation and cleared from the ASIC upon readout. CCD systems also have added blurring between pixels due to the spread of photons in the phosphor. Figure 4a) shows an image taken with the PAD of a focused electron beam with logarithmic intensity scale to show low-intensity variations. The beam saturates a 2x3 pixel area with a less intense halo extending to the upper right. The same image with a linear intensity scale is shown in Figure 4b). Figure 4c) shows a line profile along the dotted line through column 11 of the image in Figure 4b) showing a sharp drop off in intensity between pixels 10 and 11, which indicates no cross-talk, despite saturation of pixel 10.

For a single 120keV electron, the measured signal-to-noise ratio (S/N) is ~0.5, ruling out single electron detection and complicating quantitative electron beam intensity measurements. Considerable noise is introduced by the support hardware due to imperfect grounding between the analog-to-digital

converter (ADC) and PAD, temperature fluctuations, and interference in the analog output line. An equivalent S/N > 2 was achieved for this PAD using a different set of external support hardware, but space constraints of the detector canister limited choices to noisier equipment when interfaced with the electron microscope. A newer generation PAD, the mixed mode PAD (MMPAD), readily adaptable for electron detection, has a predicted single electron S/N > 20 and a well depth of $10^6 - 10^7$ 120keV HEE. [10]

The PAD tested contains twenty unresponsive pixels, likely due to bad bump bond connections. These include the entire top row of the detector, reducing the active area to 15x16 pixels. The diffraction pattern acquired with the PAD in Figure 5 shows four additional dead pixels marked by white crosses. The reduced active area of this prototype is unfortunate, but for demonstration purposes does not significantly affect the PAD operation.

5 Results and Discussion

STEM images are composed of one pixel per raster position with an intensity value dependent on the transmitted electron flux incident on a post-specimen detector. Traditional “point” (single channel) STEM detectors exist in two configurations, representing different imaging modes, which integrate the information rich diffraction pattern over their area to produce each position's image intensity. Bright field (BF) images are generated from a disk-like detector that collects electrons scattered within 0-30mrad of the central, unscattered beam. Bright field detectors produce coherent images dominated by diffraction conditions within the sample. An annular detector collects highly scattered electrons (>50mrad) to generate annular dark field (ADF) images with incoherent contrast that varies with the material's atomic number.

For each STEM raster position, the PAD collects a 15x16 pixel diffraction pattern, which is post-processed by sub-region integration or cross-correlation to yield one intensity value of the overall STEM image. This allows efficient replication of BF and ADF imaging modes and also enables novel imaging techniques based on the material's crystalline structure. Terminology ambiguities for new techniques arise between STEM images and PAD diffraction patterns, however. As a matter of definition in this paper, “position” refers to the STEM raster location on the sample, and “pixel” refers to the location of intensity

on the PAD. Data collected by the PAD are referred to as diffraction patterns while visualizations, similar to traditional STEM images, generated by processing the diffraction patterns are referred to as images.

5.1 Comparison with Traditional Imaging Techniques

The well known diffraction pattern of <110> oriented Si shown in Figure 5 demonstrates the direct electron detection capabilities of the PAD for a 120keV beam. The central beam and six diffracted beams are well localized, indicating limited pixel cross-talk and damage. Obtaining similar diffraction patterns with CCD systems requires blocking of the central peak to reduce image artifacts and detector damage. The peaks occur at known Si Bragg angles and allow determination of the solid angle the PAD subtends within the electron column for size comparisons with the standard STEM BF and ADF detectors.

Next, a 50nm-thick polycrystalline Cu film was used to test imaging methods utilizing the full diffraction patterns at each raster position acquired with the PAD. Small 50nm Cu grains are known to extend throughout the film thickness such that the focused electron beam only encounters one crystal per raster position, except near grain boundaries. Figure 6 shows STEM images from two 100x200 position rasters over a 72.5x37.5nm rectangular area of the polycrystalline Cu sample. The figures compare a) ADF and b) BF images generated from the PAD data recorded in 20 seconds (1msec/position) with those acquired using the traditional c) ADF and d) BF detectors recorded in 0.64 seconds (32μsec/position). For the PAD data, each diffraction pattern was divided into inner and outer sub-regions, similar in shape to BF and ADF detectors, and these regions were integrated to produce STEM image intensities. Images generated from the central sub-region are referred to as PAD bright field (PAD-BF), and images generated from the outer sub-region are labeled PAD annular dark field (PAD-ADF). The images show that the PAD yields equivalent physical information to traditional STEM detectors. The PAD-STEM images have higher signal-to-noise (S/N) than the poor quality traditional STEM images only due to their longer dwell time per position. The PAD-STEM images also include positions with gray levels uncorrelated with surrounding positions (known as salt-and-pepper noise), which is a consequence of inaccurate software timing for the dwell time at each raster position. This noise is not an intrinsic property of the PAD and could be eliminated by using more accurate hardware timing.

Post-acquisition integration of diffraction pattern sub-regions allows control over the electron scattering angles used to produce PAD-BF and PAD-ADF images. Images from multiple scattering ranges can be produced from a single raster, and image contrast for desired scattering conditions can therefore be maximized during post-processing analysis. Traditional STEM BF and ADF detectors have a set integration range for each raster, which is considerably less efficient. This prototype PAD is too small to collect electrons scattered to high angles typically covered by a high angle annular dark field detector (HAADF) [11], but full scale PAD chips are large enough to collect electrons within these ranges.

5.2 Novel Imaging Techniques

With a STEM, the PAD allows rapid acquisition of electron diffraction patterns, each consisting of a specific distribution of diffraction peaks that varies distinctively with the local crystalline orientation of the target material relative to the electron beam [12]. Figure 7 shows a 20x20 PAD-ADF image (with an overlaid vector field discussed later) next to two full diffraction patterns from the regions marked A and B representing separate, misaligned crystalline grains. PAD-ADF image contrast does not portray the difference between these two grains, because integration of the outer pixel sub-region of each pattern yields similar intensities for both regions. To differentiate grains, each diffraction pattern is mapped onto a two-dimensional vector capable of simultaneously representing intensity and spot pattern orientation. The vector-field components at each raster position $\vec{I}_{ij}$ are calculated from the corresponding diffraction pattern as the sum of every pixel's position relative to the main beam weighted by its intensity. Equation 1 presents this method:

$$\vec{I}_{ij} = \frac{\sum_P I_p^{ij} \vec{q}_p}{\sum_P I_p^{ij}} \tag{1}$$

where the sums are over a subset of pixels *P* on the PAD, I_p^{ij} is the intensity of pixel *p* in the diffraction pattern associated with the (i, j) position of the raster and $\vec{q}_p$ is a vector from the center beam to the pixel *p*. The vector-field overlaying the PAD-ADF image in figure 7 faithfully represents the diffraction peak orientation relative to the main beam for the included diffraction patterns and clearly distinguishes

between the two grains, demonstrating the sensitivity of the technique to slight diffraction pattern variations.

A vector field is difficult to display for large, dense STEM rasters because of limited space to properly plot every vector. An alternative visualization method to compactly represent the same information utilizes a hue/saturation value (HSV) color wheel whose hue and saturation indicate directionality and magnitude respectively. This orientation imaging representation is common in electron back scatter diffraction (EBSD) mapping [13], although the prototype PAD detector lacks sufficient resolution for full pattern indexing. Figure 8 (color online) shows the data of the PAD-ADF of Figure 6, but the image is in a vectorized color format. Individual grains and their boundaries are easily discerned while preserving vector orientation information with reference to the HSV color wheel included in the upper right corner.

Sub-region integration of PAD data does not fully utilize the information available, and vectorization of diffraction patterns may not produce unique results. An alternative technique, well suited to automated computer analysis, involves calculating the cross-correlation coefficient of diffraction patterns to quantify their similarity. An intuitive visualization to identify grain boundaries and regions with similar crystalline properties is produced by cross-correlation between second nearest neighbor positions along rows and columns. Nearest neighbor correlations tend to yield poor grain contrast, because the electron beam interacts with the adjoining crystalline structures at grain boundaries to produce a complex diffraction pattern. Figures 9a) and 9b) show images whose intensities are proportional to cross-correlation coefficients of horizontal and vertical second nearest neighbors, respectively. The method successfully separates out regions of continuous crystallinity and highlights grain boundaries. Small fluctuations in the position of intense diffraction spots incident on pixel edges can shift the spot between neighboring pixels, which produces positions with correlation coefficients that do not match surrounding positions evident as noise in Figure 9a-c). Higher PAD pixel density would increase the stability of the cross-correlation coefficient algorithm by lowering the relative importance of the intensity of each pixel. Figure 9c) is the position-by-position intensity product of figures 9a) and 9b) showing the combined

vertical and horizontal grain boundaries. Common computer algorithms are capable of determining the area of each separated grain allowing quick determination of the grain size distribution.

Figure 10 consists of three images whose intensities are proportional to the cross-correlation of a diffraction pattern at one position (marked with an X) against all other positions. Positions exhibiting high intensity are either from the same crystal or from separate crystals coincidentally aligned to produce similar diffraction patterns. The position chosen for figure 10a) reveals all other positions contained within one grain, but figure 10b) shows how two grains with similar diffraction patterns produce equivalent intensities, which complicates automated grain registration. The two grains are easily differentiated using available common computer algorithms, but coincidently aligned adjacent grains would be difficult to separate. Comparisons of patterns from grain boundaries and amorphous regions, as shown in Figure 10c), complicate creation of a fully automatic cross-correlation based algorithm sufficiently stable to produce reliable grain size distributions; however, interactive semi-automated methods are possible. Much interest lies in quickly determining a material's grain size distribution, and more refined algorithms can take advantage of the data generated by the PAD.

6 Conclusion

The 16x16 PAD tested is a hybrid detector capable of quickly acquiring the transmitted electron diffraction pattern at each position in a STEM raster scan. It proved radiation resistant to extended 120-200keV electron beam exposure (at least 10hours overall) without significant pixel cross-talk or afterglow. It replicates standard BF and ADF STEM imaging modes with post-acquisition control over the image contrast mechanisms. Preservation of the spatial distribution of intensity in the diffraction pattern enables novel imaging methods based on the crystalline structure at each raster position with application to automatically determining the material grain size distribution. The PAD could conceivably be utilized for other imaging techniques such as scanning confocal microscopy without physically descanning the transmitted beam [14] and Lorentz microscopy [15]. An optimized PAD would improve existing STEM capabilities while allowing for novel STEM applications to important materials problems.

7 Acknowledgments

We thank Lucas Koerner, Dan Schuette, Martin Novak, Gil Tombes and John Grazul for assistance. Detector research is supported by U.S. Dept. of Energy grants DE-FG- 0297ER14805 and DE-FG-0297ER62443 to SMG. Electron microscopy research is supported by the Semiconductor Research Corporation (SRC) and the Cornell Center for Materials Research (CCMR). We also benefited from equipment donated from Fischione Instruments.

Figure captions

1. Schematic cross-section of the diode structure of one pixel and its bump bond connection to the CMOS ASIC. Features are not drawn to scale but are labeled with relevant dimensions. A high energy electron incident from the top generates electron-hole pairs in the detection layer which are quickly separated by the applied reverse bias voltage. Holes are swept toward the lower contact where charge is collected and integrated by the ASIC.

2. Simulation of electron scattering from a custom written Monte-Carlo simulation including relativistic corrections based on Joy's work [8] with contour lines marking the extent of b, d) 120keV and a, c) 200keV incident electrons' energy deposition in Si. The nested contours indicate areas that contain 5%, 10%, 50%, 75%, 90% and 99% of all deposited energy, respectively, from inside out. Side views in a) and b) predict negligible energy deposition in the ASIC, which is protected by the diode layer thickness. The top view of one pixel shows energy is deposited in neighboring pixels for c) 200keV but not d) 120keV incident electrons. 120keV electrons are expected to have a smaller point spread function compared to 200keV electrons, based on the extent of electron scattering and energy deposition within the detection layer.

3. A plot of the mean response for all PAD pixels during uniform electron illumination. The measured signal shows a highly linear response to integration time up to 4ms, and hence total signal, over the detector dynamic range. Similar studies of detector response for finer integration time resolutions, not included, confirm the linearity. Saturation occurs in this figure after about 4ms exposure.

4. a) Image of a focused electron beam incident on an area of the PAD detector with logarithmic intensity scale to show low-intensity variations. The beam profile is not symmetric and consists of a main focused beam contained within a 2x3 pixel area with a coma to the upper right. b) The same image of a focused electron beam with linear intensity scale. c) Line profile of the 11th column of the PAD image showing

the actual intensity of each pixel. The large intensity difference between pixel 10 and 11 indicates excess charge in saturated pixels is not shared with neighboring pixels.

5. Diffraction pattern of the Si <110> crystalline axis collected with the PAD. The unscattered, central beam saturates the center pixel, but little intensity spreads to its neighbors. Non-functioning, dead pixels are marked with white X's. The diffraction pattern is averaged from 8,000 separate integrations collected at approximately 1.1kHz.

6. a) PAD annular dark field (PAD-ADF) and b) PAD bright field (PAD-BF) images generated by integrating the PAD's outer and inner subregions respectively. The complementary images produced with standard c) annular dark field (ADF) and d) bright field (BF) STEM detectors. Similarities between the two sets of images show that the PAD reliably reproduces the image contrast of standard STEM point detectors. The normal STEM and PAD STEM images were acquired by a FEI Tecnai T12 at 120keV with 32μsec/position and 1msec/position respectively. The traditional STEM images are significantly noisier than the PAD images only due to the large discrepancy in dwell time.

7. A PAD-ADF image overlaid with the vectors produced from the diffraction patterns collected at each position in a STEM raster (Tecnai T12 120kev, 1msec/position). Included are diffraction patterns averaged from positions within the regions marked A and B in the PAD-ADF image. There is little PAD-ADF image contrast between the regions, but the vector field indicates they are separate grains. The vectors' orientations in the image match the diffraction spot orientations in A and B. The vector field highlights the differences between misaligned crystalline grains that exhibit similar PAD-ADF image intensities.

8. (color online) A visualization generated from the diffraction spot orientation at each raster position mapped onto a color wheel. Each position's hue and saturation represent the vector field's direction and magnitude respectively. Regions of similar color and saturation originate from the same grain or from separate grains that coincidentally produce a similar diffraction pattern. Compare this visualization with

the PAD-ADF and PAD-BF images in Figure 6a-b) generated from the same PAD data. This technique more compactly displays the same information as the vector field representation of Figure 7a).

9. Image intensities correspond to cross-correlation coefficients between a) horizontal and b) vertical second-nearest neighbors. Whiter intensities indicate higher correlation and are scaled to maximize contrast. Image contrast arises from diffraction pattern variation for raster positions in differently oriented crystalline grains, unlike the PAD-ADF and PAD-BF images of Figure 6a-b). Dark bands surround differently oriented grains due to significant differences in diffraction patterns on either side of a grain boundary. c) The position-by-position product of the intensities from a) and b) showing all of the grain boundaries together. The grain structure matches that seen in Figure 8 and 10. Intensities of positions uncorrelated to its neighbors are due to small fluctuations in the collected diffraction pattern, which causes a large change in the calculated cross-correlation coefficient. A higher pixel density PAD would lower the relative importance of the intensity of single pixels and increase the stability of the cross-correlation.

10. Image intensities correspond to the cross-correlation coefficients between the diffraction pattern from the X marked position and all other positions. White intensities indicate positions exhibiting a diffraction pattern similar to the X position. This will typically indicate a) all raster positions from one single grain but b) may include similarly oriented positions within other grains. c) Cross-correlation analysis for an amorphous region shows high correlation with other amorphous regions and low correlation with crystalline grains.

References

[1] M. Watanabe and D. B. Williams, in Development of Diffraction Imaging for Orientation Analysis of Grains in Scanning Transmission Electron Microscopy, Microscopy and Microanalysis, Ft. Lauderdale, Florida, USA, 2007 (Cambridge University Press), p. 962CD.

[2] N. J. Zaluzec, in Quantitative Measurements of Magnetic Vortices Using Position Resolved Diffraction in Lorentz STEM, Microscopy and Microanalysis Conference, Quebec City, Quebec, Canada, 2002 (Cambridge University Press), p. 376 - 377.

[3] E. Heijne and P. Jarron, Nuclear Instruments and Methods in Physics Research A 275, 467-471 (1989).

[4] A. Ercan, M. W. Tate, and S. M. Gruner, Journal of Synchrotron Radiation **13,** 110-113 (2006).

[5] M. J. Renzi, Pixel Array Detectors for Ultra-Fast Time-Resolved X-ray Imaging, Thesis, Cornell University, 2003.

[6] L. Pages, E. Bertel, H. Joffre, and L. Sklavenitis, Atomic Data 4, 1-27 (1972).

[7] G. McMullan, D. M. Cattermole, S. Chen, R. Henderson, X. Llopart, C. Summerfield, L. Tlustos, and A. R. Faruqi, Ultramicroscopy 107, 401-413 (2007).

[8] Joy, D. (1995). Monte Carlo Modeling for Electron Microscopy and Microanalysis. New York: Oxford University Press.

[9] C. A. Klien, Journal of Applied Physics 39, 2029-2038 (1968).

[10] W. Vernon, M. Allin, R. Hamlin, T. Hontz, D. Nguyen, F. Augustine, S. M. Gruner, N. H. Xuong, D. R. Schuette, M. W. Tate, and L. J. Koerner, in First Results From the 128x128 Pixel Mixed-Mode Si X-Ray Detector Chip, SPIE Optics and Photonics Conference, San Diego, CA (2007).

[11] E. J. Kirkland and M. G. Thomas, Ultramicroscopy 62, 79-88 (1996).

[12] P. B. Hirsch, A. Howie, R. B. Nicholson, D. W. Pashley, and M. J. Whelan, Electron Microscopy of Thin Crystals (Butterworths, London, 1967).

[13] D. Dingley, Journal of Microscopy 213, 214 - 224 (2003).

[14] N. J. Zaluzec, Microscopy Today 11, 8-12 (2003).

[15] A. Petford-Long and J. Chapman, in Magnetic Microscopy of Nanostructures, edited by H. Hopster and H. P. Oepen (Springer-Verlag, Berlin, 2005).

Figure 1

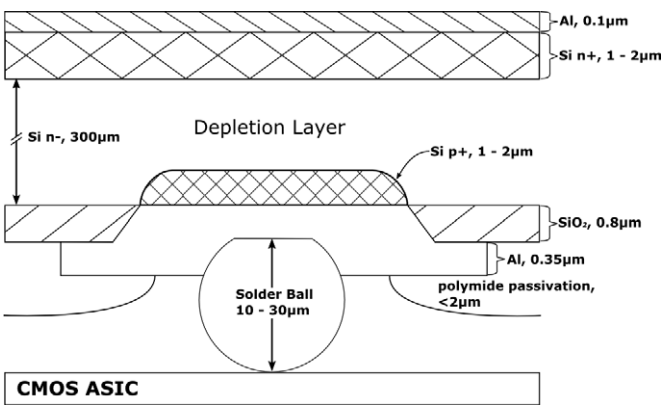

Figure 2

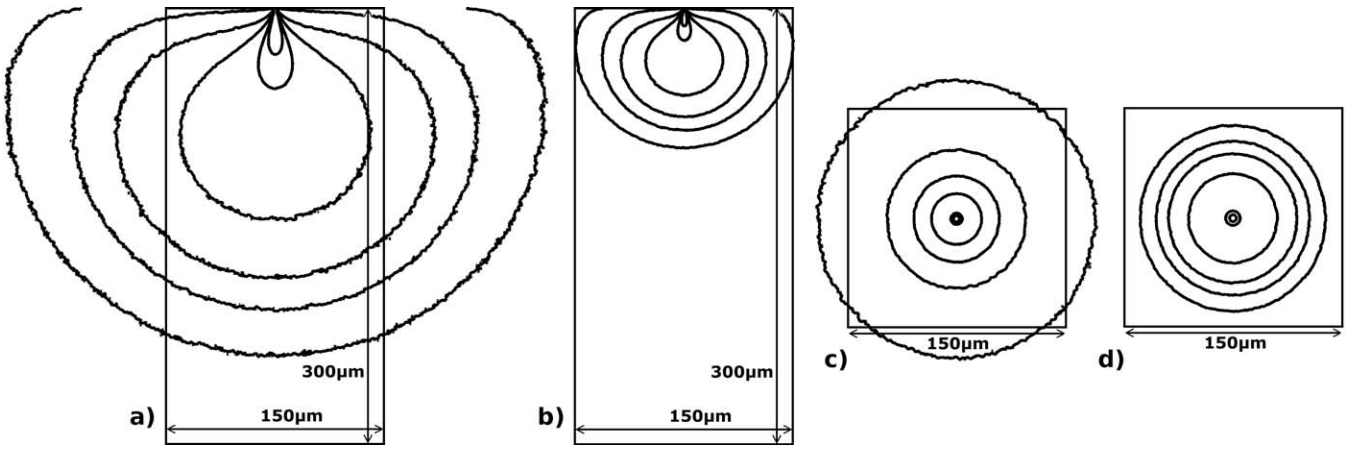

Figure 3

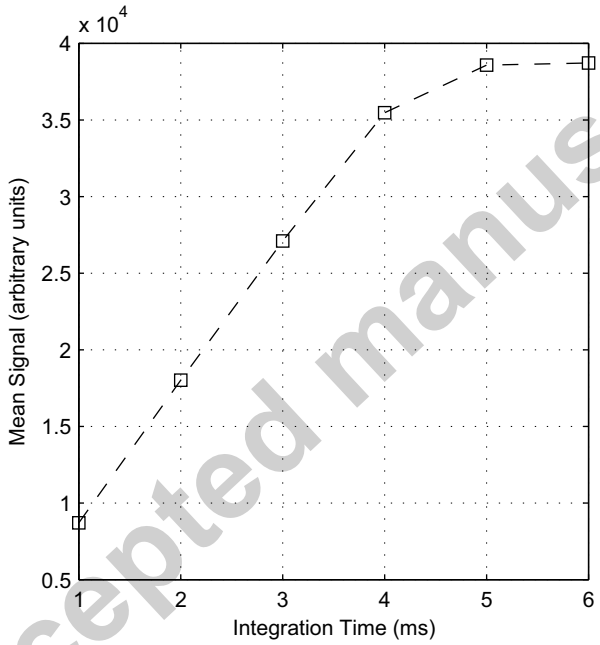

Figure 4

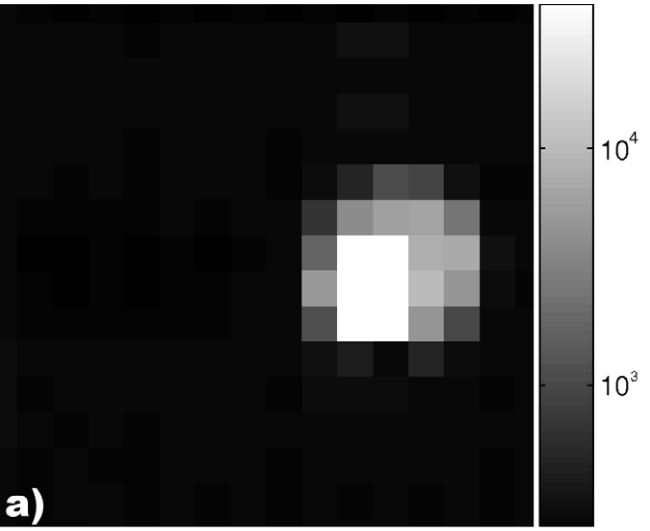

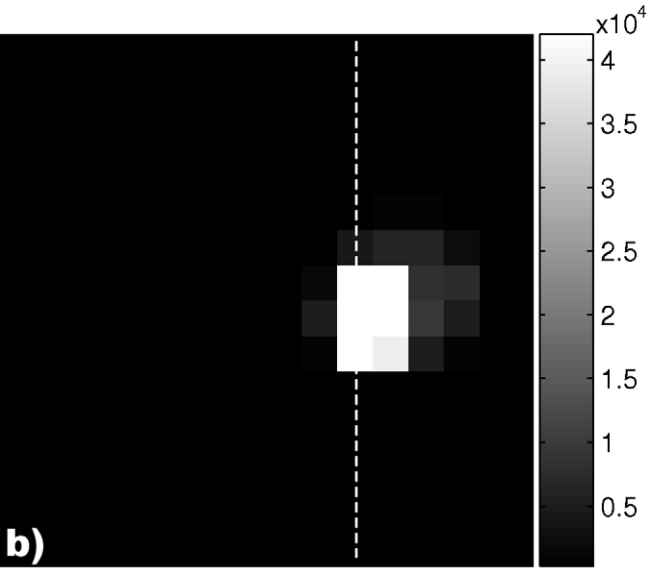

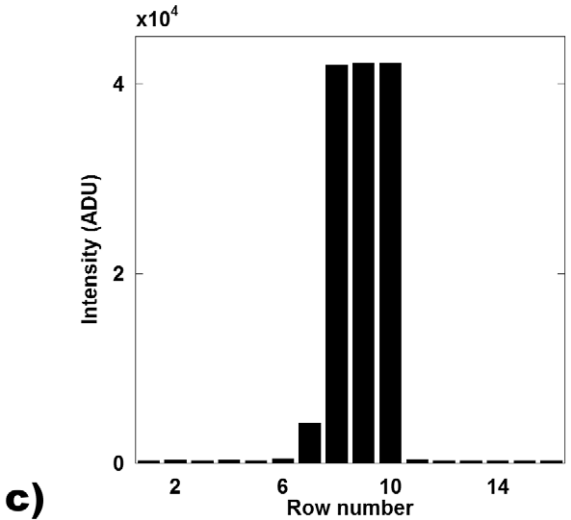

Figure 5

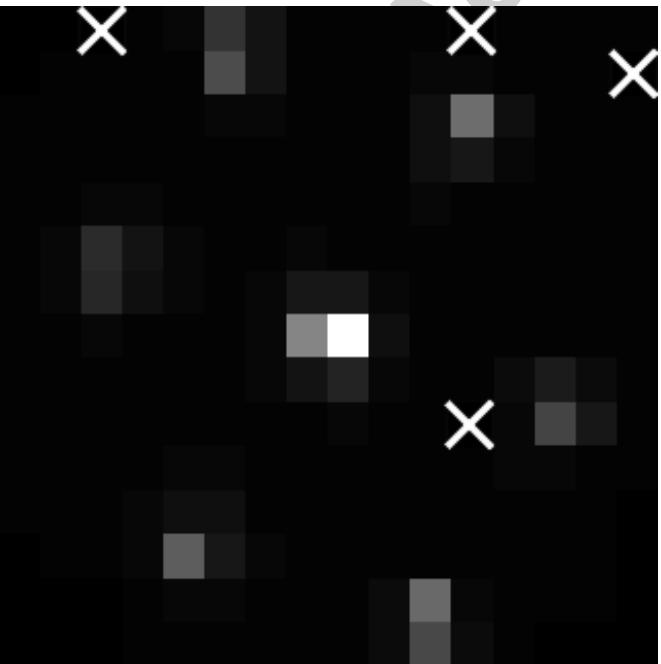

Figure 6

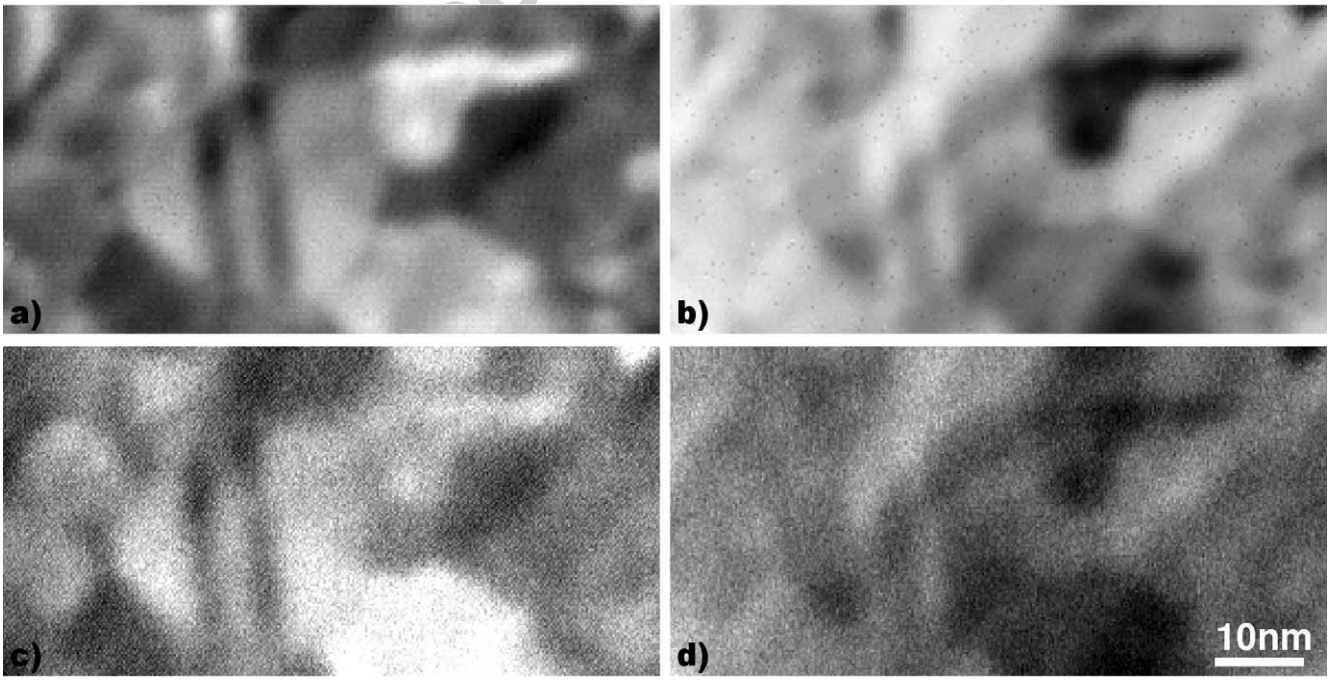

Figure 7

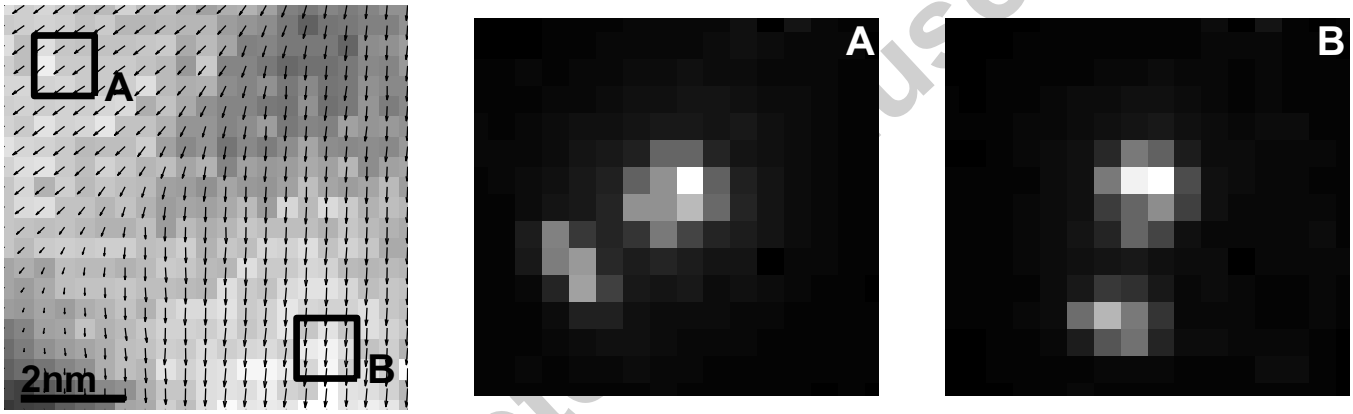

Figure 8

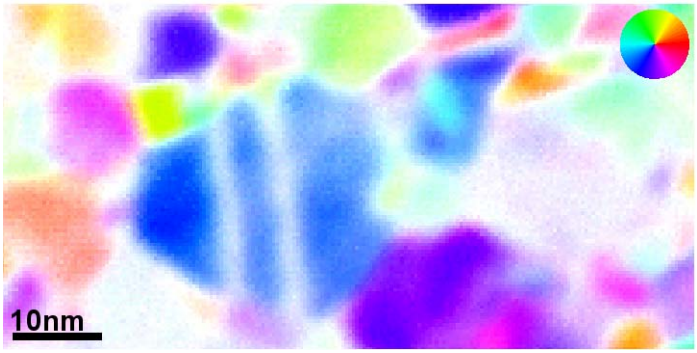

Figure 9

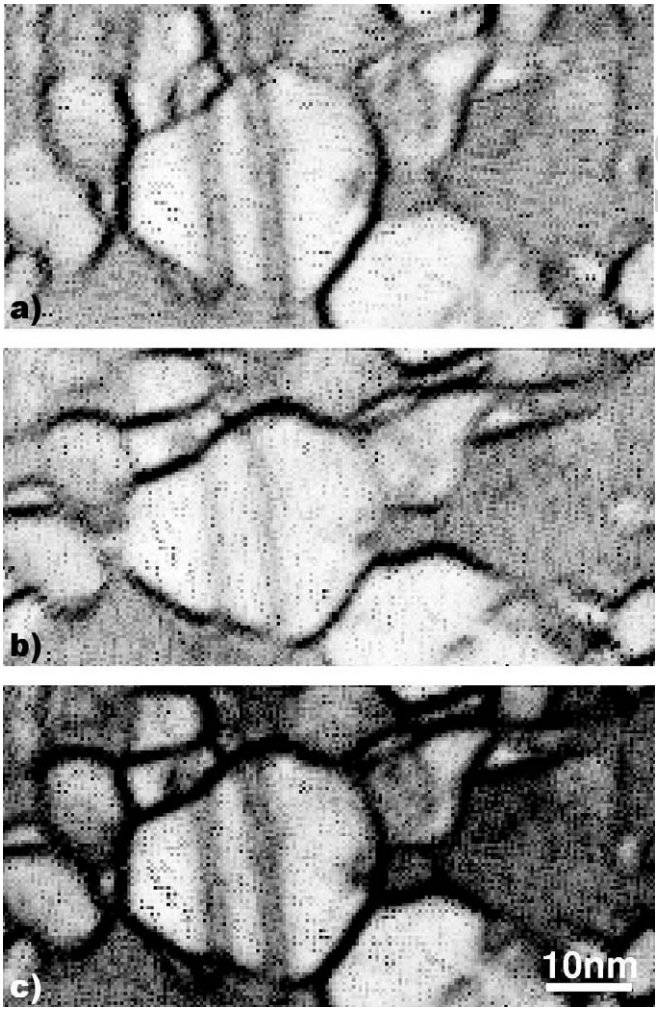

Figure 10